Supplementary Information to

Pressure-and Temperature Induced Phase Transitions, Piezochromism, NLC Behaviour and Pressure Controlled Jahn-Teller Switching in a Cu-based Framework

Charlie McMonagle[a], Priyanka Comar[a], Gary S. Nichol[a], David R. Allan[b], Jesús González[c], José A. Barreda-Argüeso[c], Fernando Rodríguez[c], Rafael Valiente[d], Gemma F. Turner[e], Euan K. Brechin[a*] and Stephen A. Moggach[e*]

a. School of Chemistry and Centre for Science at Extreme Conditions, The University of Edinburgh, King's Buildings, David Brewster Road, Edinburgh, Scotland, EH9 3FJ, UK.
b. Diamond Light Source, Harwell Campus, Didcot, OX11 ODE, UK.
c. MALTA Team, CITIMAC, Facultad de Ciencias, University of Cantabria, 39005 Santander, Spain
d. Applied Physics Dept., Facultad de Cienicas, University of Cantabria – IDIVAL, 39005 Santander, Spain
e. School of Molecular Sciences and Centre for Microscopy, Characterisation and Analysis, University of Western Australia, 35 Stirling Highway, Crawley, Perth, 6005, Western Australia, Australia

1. Synthesis

Bis[1-(4-pyridyl)butane-1,3-dione]copper(II) [$Cu(C_9H_8NO_2)_2$] (hereafter referred to as CuPry-I), was synthesised from $CuSO_4$ (0.2 mmol) dissolved in DCM (10 mL) and added to a solution of GdL_3 (0.2 mmol, where HL = 1-(4-pyridyl)butane-1,3-dione) in MeOH (10 mL). The reaction mixture was stirred for 1 hr before being filtered and diffused from diethyl ether. Green rod-like crystals formed after 4 days suitable for single crystal X-ray diffraction.

2. High pressure Single-Crystal X-ray Diffraction Experiments

High pressure experiments were performed using a Merrill-Bassett diamond anvil cell (DAC) with a half opening angle of 40° equipped with 600 μm culet Boehler-Almax cut diamonds, tungsten-carbide backing discs and a tungsten gasket.[1,2] A single crystal of the sample with a small chip of ruby (as the pressure calibrate) were loaded into the DAC using either methanol (MeOH), Fluorinert (FC-70) or *n*-pentane as a hydrostatic media. The ruby fluorescence method was used to measure the pressure throughout the experiment.[3]

3. High-pressure Laboratory and Synchrotron Data Collection, Reduction and Refinement

Initially an ambient pressure and temperature dataset was collected on a dry crystal in order to have a comparison for the high pressure data, which were also collected at room temperature. A single crystal was mounted on to a three-circle Bruker SMART APEXII diffractometer with graphite monochromated MoK_α radiation (λ = 0.71073 Å) on which a hemisphere of data was collected. Integration was performed using SAINT and the absorption correction was carried out using SADABS.[4,5]

High pressure measurements were also collected on a separate crystal, on a Bruker SMART APEXII diffractometer with graphite monochromated Mo-K_α radiation (λ = 0.71073 Å) using FC-70 as a hydrostatic medium. Data collection strategies were as described by Dawson *et al*., with a step size of 0.5° and exposure time of 40 s (60 s for the last pressure point).[6] The data were collected from 0.07 GPa to 1.56 GPa. Cell indexing and data processing were carried out using the Bruker APEX II software. Integration was performed in SAINT using dynamic masks created to remove regions of the detector which were shaded by the pressure cell. The absorption corrections were carried out using SADABS.[4,5,7] The same procedure was used to collect high-pressure data using MeOH as a hydrostatic media from 0.34 to 2.70 GPa, and pentane from 0.29 to 1.61 GPa.

High-pressure single-crystal diffraction experiments using MeOH as a hydrostatic medium were also performed at the Diamond Light Source on beamline I19-EH1 using synchrotron radiation ($\lambda = 0.48590$ Å) on a four-circle Crystal Logic diffractometer equipped with a Rigaku Saturn 724+ CCD detector. Data collection strategies were based on those described by Dawson *et al*., with a step size of 0.5° and exposure time of 1 s.[6]

Cell indexing and data processing were carried out using the Bruker APEX II software.[7] Integrations were performed using SAINT and absorption corrections were carried out using SADABS.[4,5] The data were integrated using dynamic masks to not only remove regions of the detector which were shaded by the pressure cell, but also to mask intense powder rings from the tungsten gasket. Data were collected in MeOH from 0.80 to 5.40 GPa. On increasing pressure from 2.78 to 3.34 GPa, a single-crystal to single-crystal phase transition took place. The new phase, hereafter referred to as CuPyr-II, results in a doubling of the *a* and *b*-axes, though the symmetry (space group *R*-3) is maintained.

All structures from high pressure data were solved by direct methods using ShelXT.[8] All 1,2 and 1,3 distances for the ligand were restrained to the values obtained from the ambient-pressure structure determination. All metal-ligand distances and angles were allowed to refine freely, as were all torsion angles. Merging and refinement of the data were performed using CRYSTALS.[9] Residual electron density in the pores was modelled using the SQUEEZE algorithm in PLATON. Unit cell dimensions, volumes, SQUEEZE output, coordination bonds and tabulated torsion angles as specified in the main text are given below as a function of pressure using the aforementioned hydrostatic media.

All crystallographic data have been deposited with the CCDC (CCDC 1564952, 1564954-1564972 and 2008843) and can be obtained free of charge via https://www.ccdc.cam.ac.uk/structures/, or from the Cambridge Crystallographic Data Centre, 12 Union Road, Cambridge CB2 1EZ, UK (fax +441223336033; email deposit@ccdc.cam.ac.uk).

Table S1: Unit cell dimensions, volume, SQUEEZE output, including the average void volume and number of electrons per pore as a function of pressure using FC-70 as a hydrostatic liquid. The ambient data set is given for comparison.

Phase	Pressure (GPa)	*a/b* (Å)	*c* (Å)	Volume (Å³)	Average void volume (Å³)	electrons/void
CuPyr-I	ambient	26.594(3)	7.7475(9)	4745.1(12)	384	112
CuPyr-I	0.07	26.4400(6)	7.8045(2)	4725.0(2)	388	112
CuPyr-I	0.14	26.3304(7)	7.7955(2)	4680.5(3)	380	112
CuPyr-I	0.33	26.0243(5)	7.7622(2)	4552.7(2)	353	119
CuPyr-I	0.88	25.4689(16)	7.7069(6)	4329.4(6)	319	110
CuPyr-I	1.27	25.342(2)	7.7011(5)	4283.1(8)	312	138
CuPyr-I	1.56	25.258(1)	7.7047(4)	4256.4(4)	313	126

Table S2: Unit cell dimensions, volume, SQUEEZE output, including the average void volume and number of electrons per pore as a function of pressure using MeOH as a hydrostatic liquid, collected using synchrotron radiation.

Phase	Pressure (GPa)	*a/b* (Å)	*c* (Å)	Volume (Å³)	Average void volume (Å³)	electrons/void
CuPyr-I	0.52	26.453(2)	7.7499(6)	4696.5(8)	397	173
CuPyr-I	0.96	26.025(2)	7.7498(7)	4545.7(8)	371	174
CuPyr-I	1.57	25.4451(17)	7.7312(5)	4335.0(6)	336	141
CuPyr-I	2.15	25.1855(18)	7.7300(6)	4246.3(6)	341	129
CuPyr-II	2.78	49.757(3)	7.7506(5)	16618(2)	N/A	N/A
CuPyr-II	3.34	49.109(3)	7.7842(5)	16258(2)	N/A	N/A
CuPyr-II	3.77	48.844(3)	7.8050(5)	16126(3)	N/A	N/A
CuPyr-II	4.20	48.546(4)	7.8242(5)	15969(3)	N/A	N/A
CuPyr-II	4.55	48.2797(4)	7.8324(6)	15810(3)	N/A	N/A
CuPyr-II	4.90	48.055(4)	7.8469(6)	15692(3)	N/A	N/A

Table S3: Unit cell dimensions, volume, SQUEEZE output, including the average void volume and number of electrons per pore as a function of pressure using MeOH as a hydrostatic liquid, collected using a laboratory diffractometer and Mo-Kα radiation.

Phase	Pressure (GPa)	*a/b* (Å)	*c* (Å)	Volume (Å³)	Average void volume (Å³)	electrons/void
CuPyr-I	0.34	26.6200(12)	7.7505(4)	4756.4(5)	416	133
CuPyr-I	0.71	26.1591(14)	7.7544(5)	4595.4(5)	392	140
CuPyr-I	1.08	25.7864(8)	7.7459(3)	4460.5(3)	365	125
CuPyr-I	1.28	25.6002(12)	7.7386(4)	4392.2(4)	358	134
CuPyr-I	1.56	25.4345(8)	7.7363(3)	4334.2(3)	346	113
CuPyr-I	1.77	25.3023(7)	7.7337(3)	4287.8(3)	344	115
CuPyr-II	2.23	50.229(3)	7.7339(5)	16898(2)	N/A	N/A
CuPyr-II	2.70	49.766(4)	7.7685(8)	16662(3)	N/A	N/A

Table S4: Unit cell dimensions, volume, SQUEEZE output, including the average void volume and number of electrons per pore as a function of pressure using pentane as a hydrostatic liquid, collected using a laboratory diffractometer and Mo-Kα radiation.

Phase	Pressure (GPa)	*a/b* (Å)	*c* (Å)	Volume (Å³)	Average void volume (Å³)	electrons/void
CuPyr-I	0.29	26.038(3)	7.7843(10)	4570.4(10)	356	132
CuPyr-I	0.77	25.4611(55)	7.7485(20)	4350(2)	N/A	N/A
CuPyr-II	1.61	50.0176(49)	7.7483(9)	16787(3)	N/A	N/A

Table S5: Cu-N1, Cu-O1 and Cu-O2 in CuPyr-I as a function of pressure using FC-70 as a hydrostatic media. Cu-N/O distances are also given for the ambient data set for comparison.

Pressure	Cu-N1 (Å)	Cu-O1 (Å)	Cu-O2 (Å)
ambient	2.332(4)	2.024(3)	1.961(3)
0.07	2.332(5)	2.022(5)	1.960(5)
0.14	2.297(6)	2.040(6)	1.972(5)
0.33	2.198(6)	2.114(6)	1.969(5)
0.88	2.057(9)	2.164(11)	1.978(9)
1.27	2.051(8)	2.200(9)	1.977(7)
1.56	2.046(8)	2.201(10)	1.966(8)

Table S6: Cu-N1, Cu-O1 and Cu-O2 in CuPyr-I as a function of pressure using MeOH as hydrostatic media. Data is also given for the best data set at 3.34 GPa for the four symmetry independent Cu-O/N bonds in Cu-Pyr-II.

Phase	Pressure (GPa)	Cu-N1 (Å)	Cu-O1 (Å)	Cu-O2 (Å)
CuPyr-I	0.34	2.361(5)	1.988(5)	1.963(4)
CuPyr-I	0.52	2.322(5)	2.007(5)	1.961(4)
CuPyr-I	0.71	2.277(4)	2.042(4)	1.957(5)
CuPyr-I	0.96	2.227(6)	2.068(6)	1.966(5)
CuPyr-I	1.08	2.183(4)	2.113(4)	1.963(3)
CuPyr-I	1.28	2.140(5)	2.131(6)	1.959(5)
CuPyr-I	1.56	2.111(3)	2.167(3)	1.959(3)
CuPyr-I	1.57	2.108(4)	2.161(4)	1.966(4)
CuPyr-I	1.77	2.092(3)	2.183(3)	1.959(3)
CuPyr-I	2.15	2.073(5)	2.204(6)	1.952(5)
CuPyr-II	3.34	2.111(17)	2.147(24)	1.935(19)
CuPyr-II	3.34	2.108(17)	2.249(23)	1.945(20)
CuPyr-II	3.34	2.029(16)	2.260(18)	1.893(18)
CuPyr-II	3.34	2.080(15)	2.308(22)	1.838(18)

Table S7: ∠N1Cu1O2C4 and the ∠N1Cu1O1C2 torsion angles as a function of pressure using FC-70 as a hydrostatic media. Date are also given for the ambient pressure data set for comparison.

Phase	Pressure (GPa)	∠N1Cu1O2C4 (°)	∠N1Cu1O1C2 (°)
CuPyr-I	Ambient	76.0(4)	-75.9(4)
CuPyr-I	0.07	75.8(6)	-74.8(6)
CuPyr-I	0.14	74.8(6)	-75.1(6)
CuPyr-I	0.33	74.6(6)	-74.3(6)
CuPyr-I	0.88	72.2(12)	-76.1(11)
CuPyr-I	1.27	71.6(10)	-73.8(9)
CuPyr-I	1.56	70.6(11)	-73.1(10)

Table S8: ∠N1Cu1O2C4 and the ∠N1Cu1O1C2 torsion angles as a function of pressure using MeOH as a hydrostatic media**.**

Phase	Pressure (GPa)	∠N1Cu1O2C4 (°)	∠N1Cu1O1C2 (°)
CuPyr-I	Ambient	76.0(4)	-75.9(4)
CuPyr-I	0.52	69.8(5)	-70.0(5)
CuPyr-I	0.96	67.7(7)	-69.2(7)
CuPyr-I	1.57	65.4(5)	-68.8(5)
CuPyr-I	2.15	63.8(6)	-68.6(6)

4. High-pressure piezochromic behaviour using MeOH as a function of pressure.

In order to determine the reversibility of the piezochromic behaviour observed on compression of CuPyr-I in MeOH, confocal images were collected on decreasing pressure, where a red-green shift in colour was observed (Figure S1).

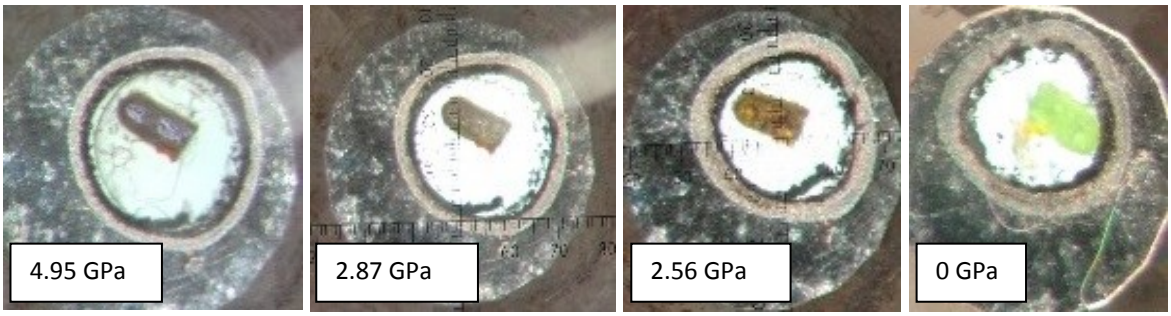

Figure S1: Confocal images of CuPyr-I in MeOH on decompression, showing the reversibility of the piezochromic effect.

5. High-pressure diffraction experiments using ethanol (EtOH) and propan-2-ol (IPA) as hydrostatic media

Following the successful compression of CuPyr-I in MeOH further high-pressure experiments using higher alcohols were attempted. Two higher alcohols that are commonly used as hydrostatic media were selected, EtOH and IPA. Upon loading a crystal in EtOH the crystal

rapidly split. This splitting continued over only a few minutes until the crystal had fully disintegrated making the collection of high-pressure data impossible. On loading a separate sample in IPA, similar behaviour was observed, with the crystal losing colour, eventually becoming amorphous over the course of 2-3 hours (Figure S2).

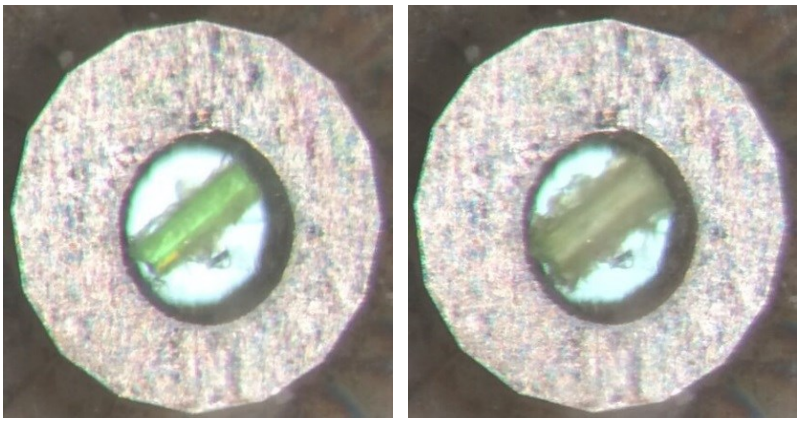

Figure S2: Confocal microscopy images of a loaded diamond anvil cell (DAC) loaded with CuPyr-I using IPA as a hydrostatic media after initial loading (left) and after 12 hours (right).

6. Synthetic Precession Images

The phase transition from CuPyr-I to CuPyr-II was identified by inspecting synthetic precession images of the *hk0* plane. As the transition resulted in a doubling of the *a* and *b* axes, twice the number of reflections appear on this plane, and can therefore be easily identified using these images, making the CuPyr-II phase transition simple to identify. All of these images

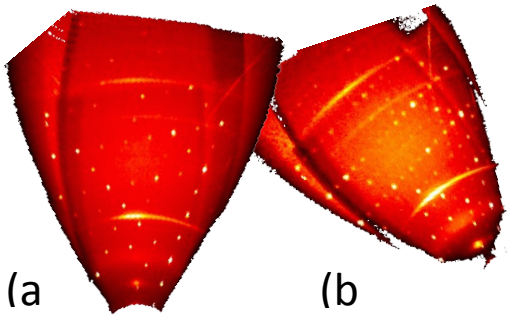

were created using the Bruker APEX II software suite.[7]

Figure S3: Precession image of the hk0 plane at (a) 1.77 GPa and (b) 2.23 GPa using MeOH as a hydrostatic media.

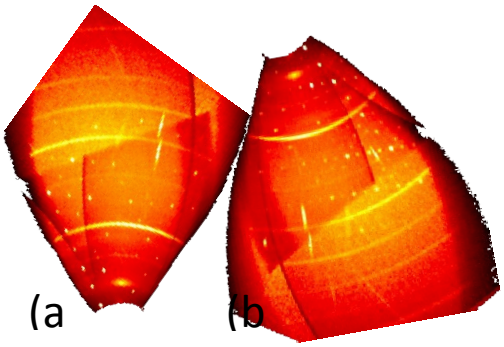

Figure S4: Precession image of the hk0 plane at (a) 0.29 GPa, and (b) 0.77 GPa using n-pentane as a hydrostatic media.

7. Variable Temperature Single Crystal X-ray Diffraction Measurements

Variable temperature single-crystal data were collected with a three-circle Bruker SMART APEXII diffractometer with graphite monochromated MoK_α radiation (λ = 0.71073 Å). Data were collected from 300 to 100 K in 50 K steps. Cell indexing and data processing were carried out using the Bruker APEX II software. Integration was performed using the program SAINT while the absorption corrections were carried out using the program SADABS.[4,5] On cooling from 300 K to 150 K, short data collections were performed in order to index the crystal (Table S9). On cooling to 100 K, a single-crystal to single-crystal phase transition occurred to another, previously unobserved phase, hereafter referred to as CuPyr-III. Several attempts were required in order to obtain a crystal of CuPyr-III which was suitable for structure solution and refinement. This was obtained, in the end by taking a crystal of CuPyr-I and placing it on the instrument at 200K.

The structure of CyPyr-III was solved by Charge Flipping using the Superflip[10] structure solution program and refined in the program Olex2 using ShelXL. The structure solved in the triclinic space group P-1, (a = 7.7799(3), b = 15.1586(9), c = 15.4901(9), α = 116.604(6), β = 100.395(4), γ = 98.422(4)). The final conventional R-factor was 6.1 % for 1451 data. All non-hydrogen atoms were refined anisotropically. Hydrogen atom positions were calculated geometrically and refined using the riding model.

Table S9: Unit cell dimensions of CyPyr-I on cooling from 300 to 150 K from single-crystal diffraction data.

Temperature (K)	*a* (Å)	*b* (Å)	*c* (Å)	α	β	γ	Unit Cell Volume (Å^3)

300	26.56(1)	26.56(1)	7.708(3)	90	90	120	4709(5)
250	26.48(1)	26.48(1)	7.721(3)	90	90	120	4688(5)
200	26.42(1)	26.42(1)	7.731(3)	90	90	120	4673(5)
150	26.25(2)	26.25(2)	7.723(7)	90	90	120	4609(11)

8. Laboratory Low Temperature Powder X-ray Diffraction Measurements

Variable temperature X-ray powder diffraction data were collected on CuPry-I from 300 K to 180 K in 10 K steps, then from 180 K to 130 K in 5 K steps. The sample was loaded into a 0.7 mm glass capillary, and mounted on a Bruker D8 diffractometer using Cu Kα radiation (λ = 1.54056 Å). Data were collected from 5-50° in 2θ in 0.02° steps. On cooling below 175 K, the transition to the triclinic CuPyr-III phase was observed (Figure S5).

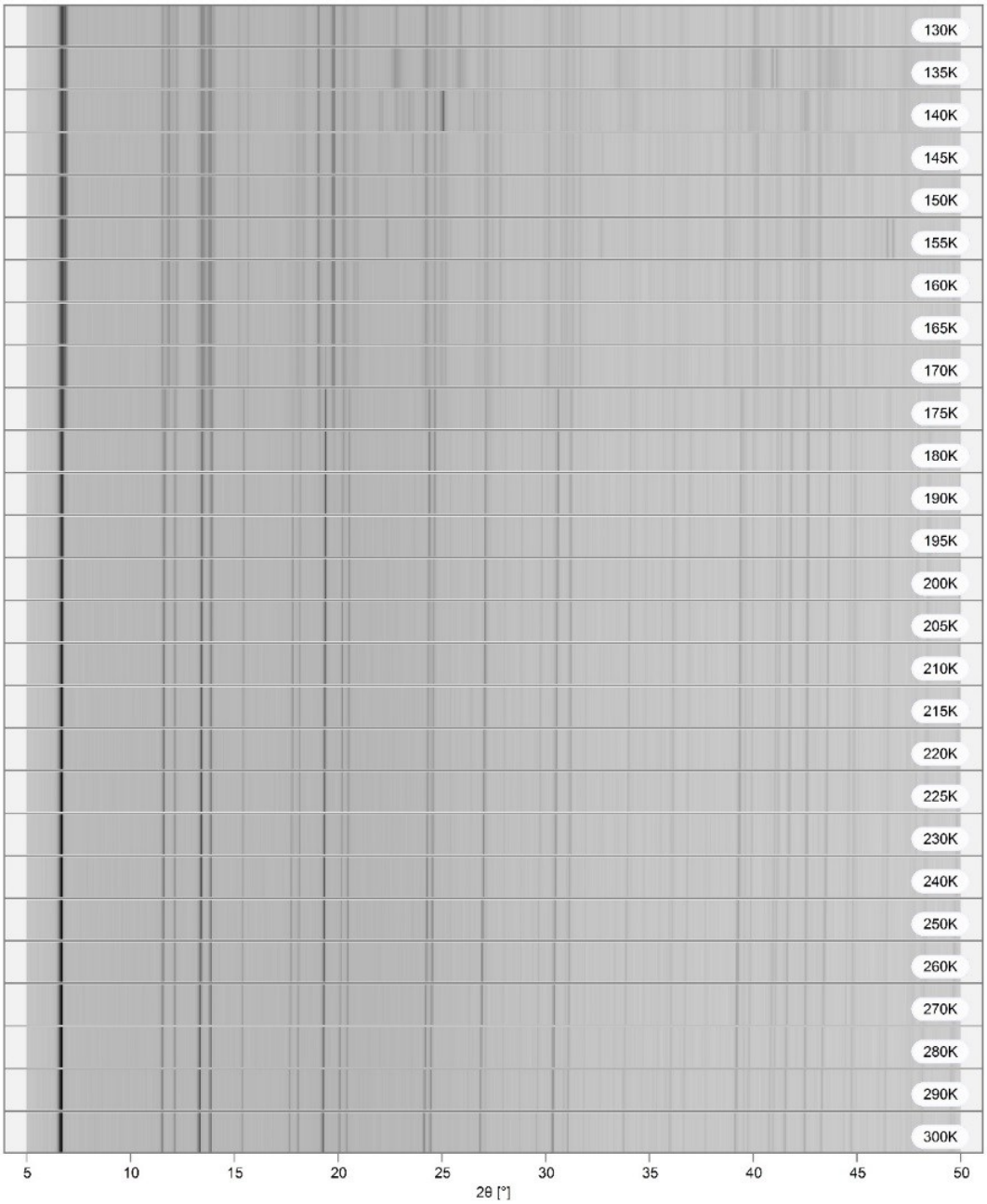

Figure S5: Powder diffraction data on CuPyr-I. Note the phase transition from CuPyr-I to CuPyr-III on cooling from 175 to 170 K respectively.

9. TGA

Thermogravimetric analysis (TGA) was performed on CuPyr-I to assess its thermal stability. A heating rate of 10 K/min was applied up to a final temperature of 550°C in an inert atmosphere of nitrogen at a flow rate of 50 ml/min. The instrument used was a Netzsch STA 449F1 fitted with a platinum furnace. Saw tooth blips on the trace are an artefact from the measurement and do not affect the two observed mass changes. The initial loss of 2.52 % at 140°C is attributed to the loss of diethyl ether present from synthesis and this is followed by the decomposition of CuPyr-I at 220°C.

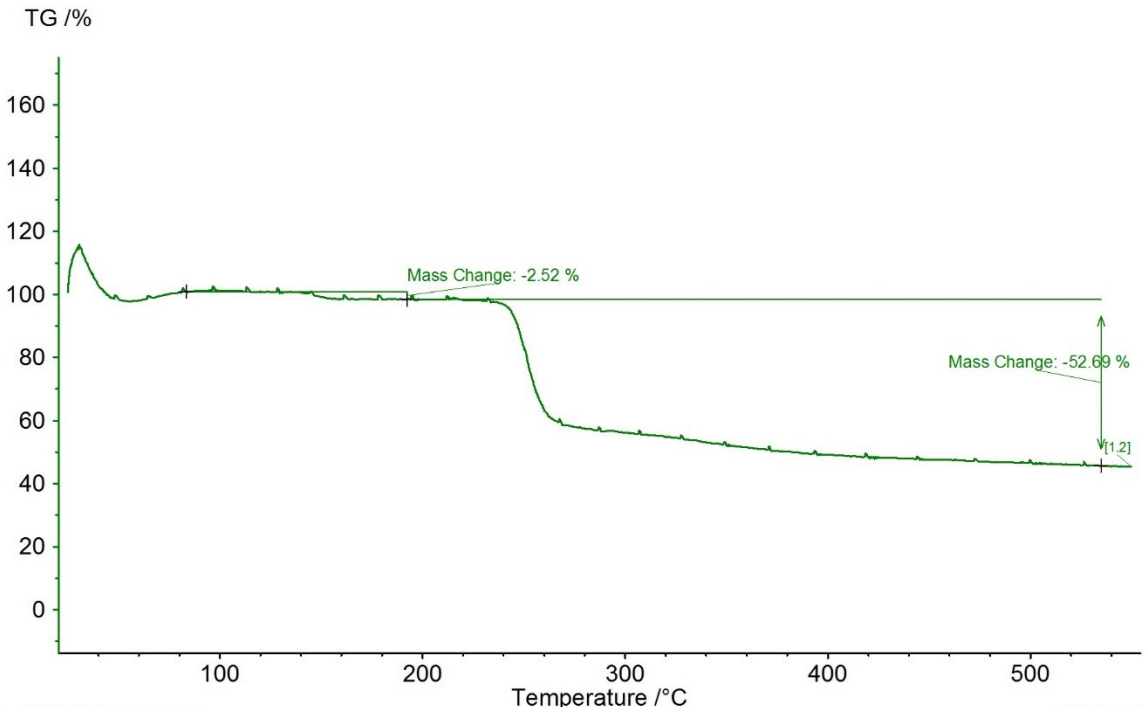

Figure S6: TGA performed on CuPyr-I.

10. UV-Visible Spectroscopy

UV-visible spectroscopy experiments from ambient pressure to 11 GPa were performed in each Fluorinert® FC-70 and methanol. The experiments were carried out in a Boehler-Almax DAC using a bespoke set-up. A tungsten light source and reflective objectives coupled to dedicated Ocean spectrometers for different spectral ranges were using to analyse the transmitted light.[12]

According to X-ray diffraction data, all copper ions lie on crystallographic inversion centres (are at centrosymmetric sites). The electronic specta in the *d-d* and charge-transfer domains can be understood within an approximate D_{2h} molecular symmetry framework of the Cu^{2+} complex. The Cu^{2+} ground state can be assigned to a state with $d_{x^2-y^2}$ character,[13] where the *z*-direction has been chosen along the Cu-N bond direction. The tentative assignment of the d-levels follows the sequence $d_{x^2-y^2} > d_{xy} > d_{z^2} > d_{yz} > d_{xz}$ characteristic of a [Cu $O_2O'_2N_2$] complex (Figure S7), and the structure may be considered as being analogous to a tetragonally elongated octahedron with two nitrogens contributing to the out-of-plane bonding at ambient conditions.[14] Within this scheme, all energy levels are non-degenerate.

Experimentally, the absorption spectra consist of a weak broad band peaking at about 700 nm (14300 cm^{-1}) associated with a *d-d* electronic transition within the [$CuO_2O'_2N_2$] complex. Similar results were observed for other Cu^{2+} systems[13-17] with oxygen and nitrogen ligands and Mn^{3+} systems with oxygen and fluorine ligands[18], both having the same elongated D_{2h} local symmetry. Additionally, a steeped absorption threshold associated with a strong band emerges below 450 nm. This absorption edge behaves as a direct band-gap absorption. The origin of this band is not clear at all, it can be due either to a ligand-to-metal charge-transfer band or to the organic ligands. Nevertheless, the comparison of this band-gap absorption and that measured in $CuMoO_4$ [19] and $CuWO_4$,[20] both having an energy gap of 2.30 eV, makes it to tentatively assign the absorption threshold to a metal-ligand charge-transfer band gap.

The absorption band gap and its pressure-induced redshift are responsible of the colour and the strong piezochromism of this crystal. Figure S8 shows the variation of absorption spectra of the Cu-MOF as a function of pressure for each methanol and fluorinert hydrostatic media.

Interestingly, the absorption spectra behave similar with pressure irrespective of the pressure transmitted medium as methanol or fluorinert. In the 0-3 GPa range, the *d-d* transition band shifts linearly with pressure to higher energies at a rate of 380±50 cm^{-1} GPa^{-1} (Figure S9), while the absorption edge shifts to lower energies, and finally both bands merge together in the visible region around 700 nm. It must be noted that the absorption edge is more sensitive to pressure than *d-d* transitions, with a red-shift rate of about –800±90 $cm^{-1}GPa^{-1}$ (-99 meVGPa^{-1}). This is one of the largest pressure shifts ever measured.[20] Hence, pressure induces a progressive and quick darkening of the sample, with the band gap being responsible of its piezochromism. Above 3 GPa the pressure shift decreases as a consequence of the sample hardening.

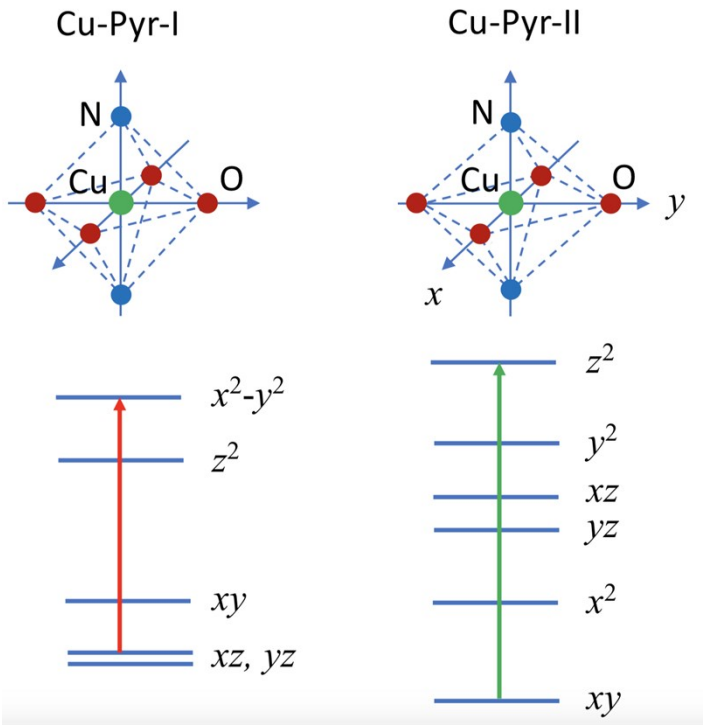

Figure S7: Schematic splitting of the *d*-energy levels of Cu^{2+} in Cu-MOF in the low and high pressure phases.

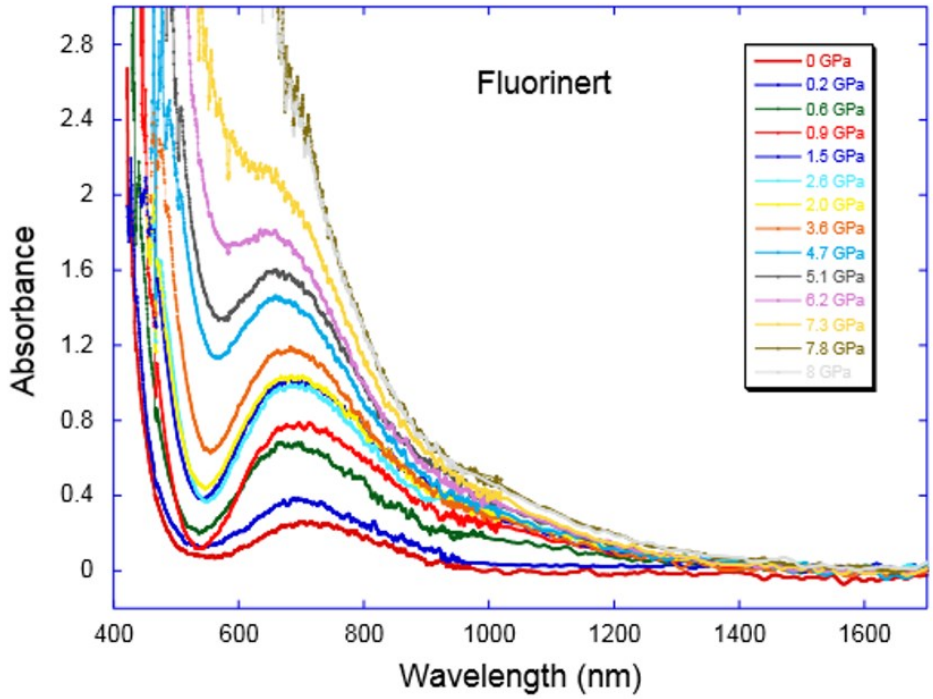

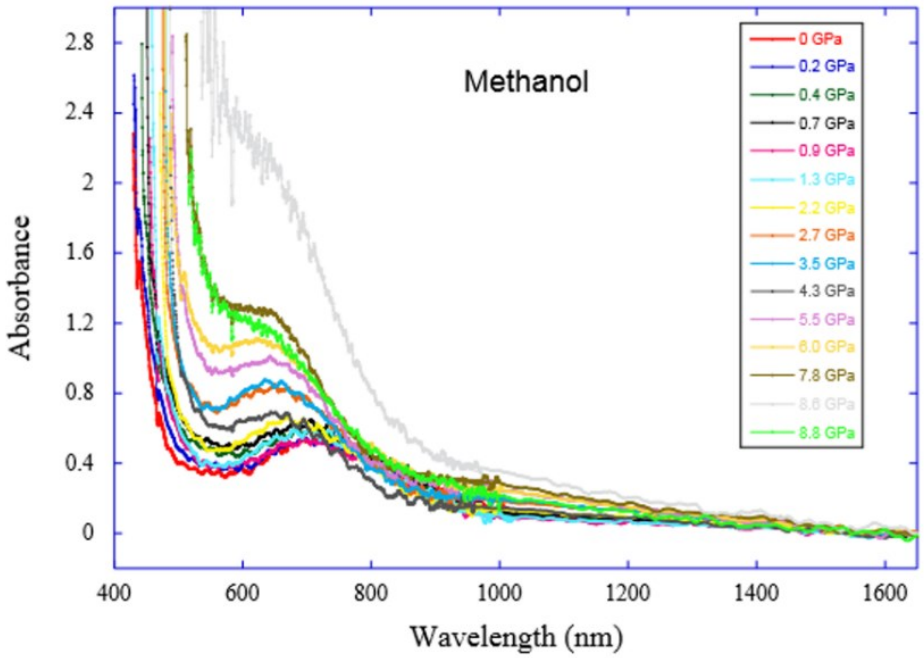

Figure S8:Variable pressure UV-visible spectra of CuPyr-I in a Fluorinert® FC-70 (top) and methanol (bottom) hydrostatic media.

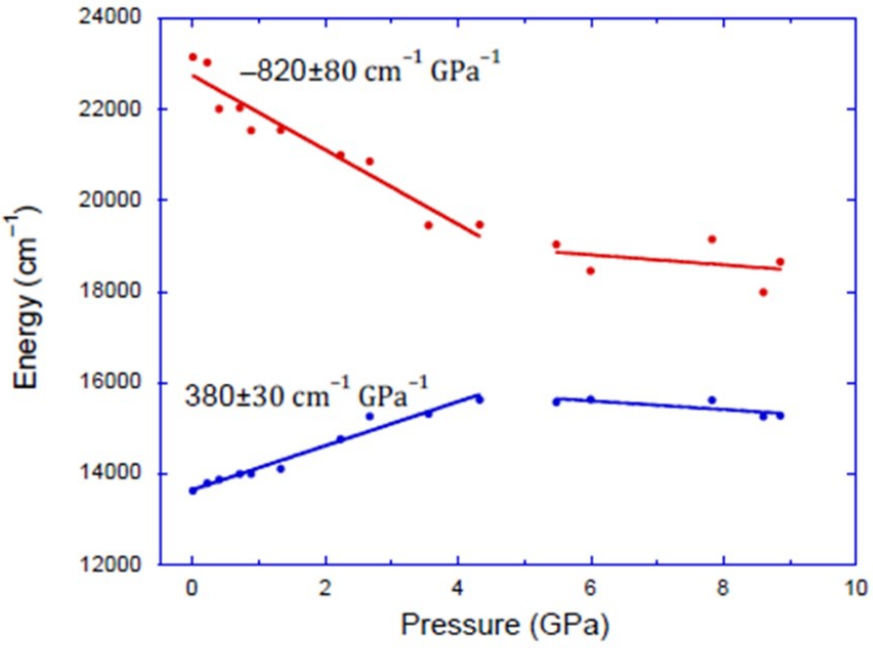

Figure S9: Variation of the peak energy (in cm^{-1} units) of *d-d* (blue) and absorption edge (red) with pressure obtained through linear least-square fitting of data from Figure S7.

11. Raman Spectroscopy

The 647 nm line of an Ar^{+}-Kr^{+} laser and triple monochromator Horiba-Jobin-Yvon T64000 equipped with a N_2 cooled CCD were used for Raman spectroscopy.

Figures S10 show the Raman spectra of Cu-MOF as a function of pressure usingmethanol as pressure transmitting medium. The low frequency Raman peaks (50-200 cm^{-1}) can be associated with lattice modes, whereas those located between 250 and 1000 cm^{-1} are assigned to stretching Cu-N and Cu-O internal vibrations of the [$CuO_2O'_2N_2$] complex (Figure S11), according to previous measurements reported elsewhere.[21-25] Interestingly, the frequency assigned to a stretching Cu-O internal mode decreases with increasing pressure up to 1 GPa at a rate of -8 $cm^{-1}GPa^{-1}$, in contrast to the Cu-N internal mode which frequency increases at 10 $cm^{-1}GPa^{-1}$ in the same pressure range. Above 1 GPa, both modes follow the general tendency of all the other modes. This puzzling behavior can be understood on the basis of structural correlations. The pressure-induced frequency redshift of the Cu-O internal mode can be correlated with the increase in Cu-O bond length with pressure as derived from X-ray data. Frequency shifts of the remainder internal modes Cu-O' and Cu-N show the usual trends of stretching modes when the associated bond lengths decrease with pressure.

The appearance of new peaks above about 2 GPa is noteworthy. It just corresponds to same pressure at which a first-order structural phase transition was observed by X-ray diffraction. A similar behavior was shown by the optical absorption spectra but in a different pressure range. The band gap and *d-d* band energy pressure dependences show a different shift rate above and below 5 GPa, thus suggesting that although electronic transitions are not very influenced by the structural phase transition at 2 GPa, the existence of another structural phase transition at 5 GPa is likely. Although Raman spectra show additional features compatible with a phase transition at 5 GPa, further X-ray studies in this pressure range are required to confirm the spectroscopic findings. Raman spectra could not be collected for CuPyr in a hydrostatic medium of Fluorinert® FC-70 due to the strong absoprtion of the medium.

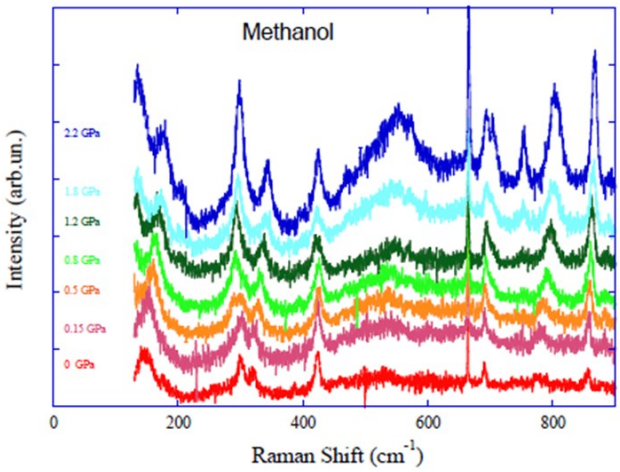

Figure S10: Pressure-dependent Raman spectra of CuPyr in a hydrostatic medium of methanol.

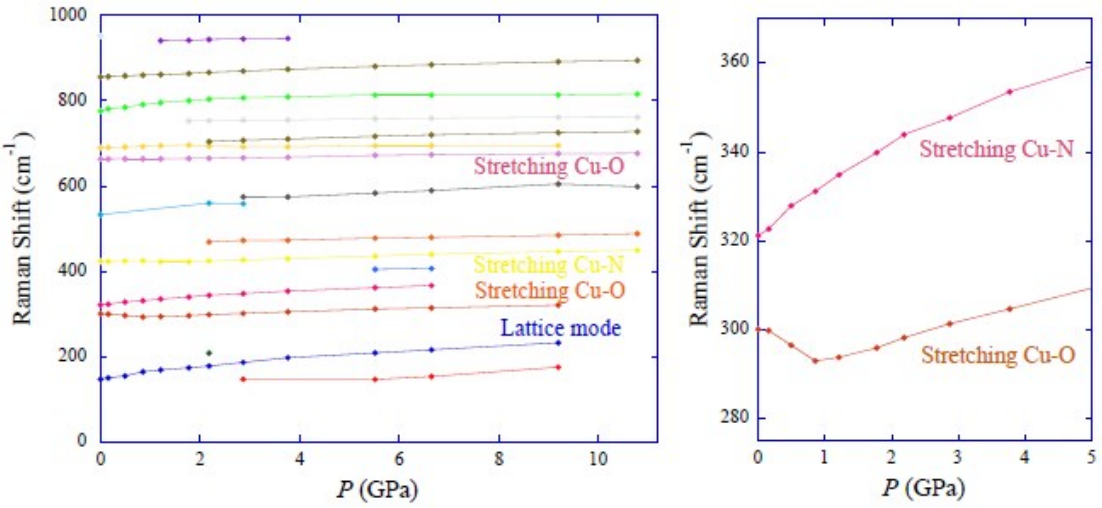

Figure S11: Variation of the vibrational frequencies with applied pressure.

References

1 Merrill, L. & Bassett, W. A. Miniature diamond anvil pressure cell for single-crystal X-ray-diffraction studies. *Rev. Sci. Instrum.* **45**, 290-294, doi:10.1063/1.1686607 (1974).

2 Moggach, S. A., Allan, D. R., Parsons, S. & Warren, J. E. Incorporation of a new design of backing seat and anvil in a Merrill-Bassett diamond anvil cell. *J. Appl. Crystallogr.* **41**, 249-251, doi:10.1107/S0021889808000514 (2008).

3 Piermarini, G. J., Block, S., Barnett, J. D. & Forman, R. A. Calibration of pressure-dependence of R1 ruby fluorescence line to 195 kbar. *J. Appl. Phys.* **46**, 2774-2780, doi:10.1063/1.321957 (1975).

4 SAINT v. 8.34A (Bruker AXS Inc., Madison, Wisconsin, USA, 2014).

5 SADABS v. 2008-1 ed. (Bruker AXS Inc., Madison, Wisconsin, USA, 2014/15).

6 Dawson, A., Allan, D. R., Parsons, S. & Ruf, M. Use of a CCD diffractometer in crystal structure determinations at high pressure. *J. Appl. Crystallogr.* **37**, 410-416, doi:10.1107/S0021889804007149 (2004).

7 APEX2 v. v2014.11-0 (Bruker AXS Inc., Madison, Wisconsin, USA, 2014).

8 Sheldrick, G. SHELXT - Integrated space-group and crystal-structure determination. *Acta Crystallogr. Sect. A* **71**, 3-8, doi:doi:10.1107/S2053273314026370 (2015).

9 Betteridge, P. W., Carruthers, J. R., Cooper, R. I., Prout, K. & Watkin, D. J. CRYSTALS version 12: software for guided crystal structure analysis. *J. Appl. Crystallogr.* **36**, 1487-1487, doi:10.1107/s0021889803021800 (2003).

10 Palatinus, L. & Chapuis, G. SUPERFLIP - a computer program for the solution of crystal structures by charge flipping in arbitrary dimensions. *J. Appl. Crystallogr.* **40**, 786-790, doi:10.1107/s0021889807029238 (2007).

11 Spek, A. L. Single-crystal structure validation with the program PLATON. *Journal of Applied Crystallography* **36**, 7-13, doi:Doi 10.1107/S0021889802022112 (2003).

12 F. Rodríguez and J.A. Barreda-Argüeso, Patent PCT/ES2014/000049.

13 Hathway, B. J. and Billing, D. E., The electronic properties and stereochemistry on mono-nuclear complexes of the copper (II) ion, *Coordination Chemistry Reviews,* **5**, 143-207, 1970 and references therein

14 R.J. Dudley, R.J. Fereday, B.J. Hathaway, P.G. Hodgson, and P.C. Power, Single-crystal electronic and electron spin resonance spectra of the two forms of bis(nitrato)bis-(a-picoline)copper(II) and of bis(nitrato)-mono(pyrazine)copper (II), J. Chem. Soc., Dalton 1044-1047 (1973)

15 The single-crystal electronic and electron spin resonance spectra of transbis(monochloroacetato)bis-(2-methylpyridinine)copper(II), J. Chem. Soc. (A) 1446 (1971)

16 Crystal structure and electronic properties of bis(2,2′-bipyridyl)-nitratocopper(II) nitrate monohydrate. R. J.Fereday, P. Hodgson, S. Tyagi, and B. J.

Hathaway, J. Chem. Soc., Dalton Trans. 10, 2070–2077 (1981).

17 Synthesis, X-ray structure, polarized optical spectra and DFT theoretical calculations of two new organic–inorganic hybrid fluoromanganates(III): (bpaH2)[MnF4(H2O)2]2 and (bpeH2)[MnF4(H2O)2]2, P. Núñez, J. C. Ruiz-Morales, A. D. Lozano-Gorrín, P. Gili, V. D. Rodriguez, J. González-Platas, T. Barriuso and F. Rodríguez, Dalton Trans. 2, 273–278 (2004).

18 Optical study of the piezochromic transition in CuMoO4 by pressure spectroscopy, F. Rodriguez, D. Hernández, J. Garcia-Jaca, H. Ehrenberg and H. Weitzel, Phys. Rev. B 61, 16497-16501 (2000).

19 Optical absorption and Raman spectroscopy of CuWO4, J. Ruiz-Fuertes, M. N. Sanz-Ortiz, J. González, F. Rodríguez, A. Segura and D. Errandonea, J. Phys. Conf. Ser. 215, 012048, 5pp (2010).

20 F. Rodríguez, R. Valiente, V. Lavín, and U. R. Rodríguez-Mendoza, Optical Spectroscopy, in An Introduction to High-Pressure Science and Technology (CRC Press, Taylor & Francis, Boca Raton, 2015) Ch. 8, pp. 219-260.

21 Vibrational study and semiempirical calculation for the hexaazacyclophane copper (II) complex, M.M. Campos-Vallette, R.E. Clavijo C., F. Mendizabal, G. Diaz F., J. Costamagna, J. Canales, J. Vargas, Vibrational Spectroscopy 14, 71-78 (1997)

22 Raman scattering of Cupric oxide (CuO), T. Wei, PhD Thesis, Simon Fraser University (1990)

23 Vibrational study of N-phenyl-substituted hydroxynaphthylaldiminate copper complexes, M. Campos-Vallette, K. Figueroa and R.O. Latorre, G. Díaz Fleming, J. Costamagna, J.C. Canales, M. Rey-Lafon, J. Derouault, Vibrational Spectroscopy 6, 25-35 (1993)

24 Vibrational Properties of CuO and Cu4O3 from First-Principles Calculations, and Raman and Infrared Spectroscopy, L. Debbichi, M. C. Marco de Lucas, J. F. Pierson, and P. Krüger, J. Phys. Chem. C 116, 10232−10237 (2012)

25 Second-order Raman scattering in CuO, A. P. Litvinchuk, A. Möller, L. Debbichi, P. Krüger, M. N. Iliev and M. M. Gospodinov, J. Phys.: Condens. Matter 25, 105402 (2013)